

Noise-Aware Saliency Prediction for Videos with Incomplete Gaze Data

Ekta Prashnani^{1,2} Orazio Gallo¹ Joohwan Kim¹ Josef Spjut¹ Pradeep Sen² Iuri Frosio¹
¹NVIDIA ²University of California, Santa Barbara

Abstract

Deep-learning-based algorithms have led to impressive results in visual-saliency prediction, but the impact of noise in training gaze data has been largely overlooked. This issue is especially relevant for videos, where the gaze data tends to be incomplete, and thus noisier, compared to images. Therefore, we propose a noise-aware training (NAT) paradigm for visual-saliency prediction that quantifies the uncertainty arising from gaze data incompleteness and inaccuracy, and accounts for it in training. We demonstrate the advantage of NAT independently of the adopted model architecture, loss function, or training dataset. Given its robustness to the noise in incomplete training datasets, NAT ushers in the possibility of designing gaze datasets with fewer human subjects. We also introduce the first dataset that offers a video-game context for video-saliency research, with rich temporal semantics, and multiple gaze attractors per frame.

1. Introduction

The human eye perceives high-frequency details within a small solid angle around the viewing direction [17, 13]. To form the mental image of a scene, the eyes explore, or “fixate on,” different regions. Predicting the spatial distribution of the human-gaze locations has applications including image or video compression [3], and foveated rendering [30, 29], among others. Early methods achieved this using low- or mid-level [24, 23, 31] image features, while recent deep-learning (DL) approaches leverage higher-level priors [22, 36, 33, 42, 49, 25, 32, 38], to obtain a saliency map: an estimate of the probability distribution of gaze over all the pixels of an image.

Capturing gaze data to train DL algorithms is becoming increasingly easy with the recent improvements in gaze-tracking technologies. However, large-scale gaze data acquisition remains a time-consuming, expensive procedure affected by a number of sources of noise, from physiological nystagmus (the involuntary jittering of the eyes), to inac-

This work was done in part when E. Prashnani was interning at NVIDIA.

curate localization of the Purkinje reflection (the reflection of the IR illuminator used to track the eye), to calibration issues [15]. Collectively, we refer to these sources of noise as *measurement noise*, which result in uncertainty about the spatial localization of the gaze of any single observer.

Capturing gaze data on videos is even more challenging: typically, only one gaze location per observer is collected per video frame. This introduces a trade-off. For a given time/cost budget, one can either collect gaze data from many observers for the same video frame to get dense saliency maps for few frames, or capture fewer gaze fixations per frame to get sparse saliency maps for many frames. As a result, the measured saliency maps of large-scale video-saliency datasets are typically based on fewer fixations per frame. We refer to this source of inaccuracies as *incomplete sampling*: we have partial observations of the underlying complete saliency map for each video frame. One effect of incomplete sampling is that the masses of different modes in a measured saliency map may be inaccurate, as they are estimated from few observations.

The complex interaction of measurement noise and incomplete sampling impact the reliability of the training gaze data in each frame, depending on the number of observers and the specific saliency map. This is particularly apparent when few observers are available, as in the case of video saliency prediction. We propose a novel training paradigm that leverages this observation by accounting for the reliability of each measured saliency map. To this aim, we introduce a simple model that quantifies the uncertainty in a measured saliency map, given the number of fixations. Instead of directly minimizing the discrepancy d between the measured and predicted saliency maps, as is typically done, we interpret d as a random variable and train the saliency predictor through likelihood maximization. We call this proposed training paradigm *noise-aware training* (NAT). Through several experiments, we show that NAT avoids overfitting towards noisy saliency maps, weighs training frames according to their reliability, and consistently yields improved saliency predictions over traditional training methods, for different datasets, deep neural networks (DNN), and training discrepancy d (Fig. 1), especially when few observers or frames are available for train-

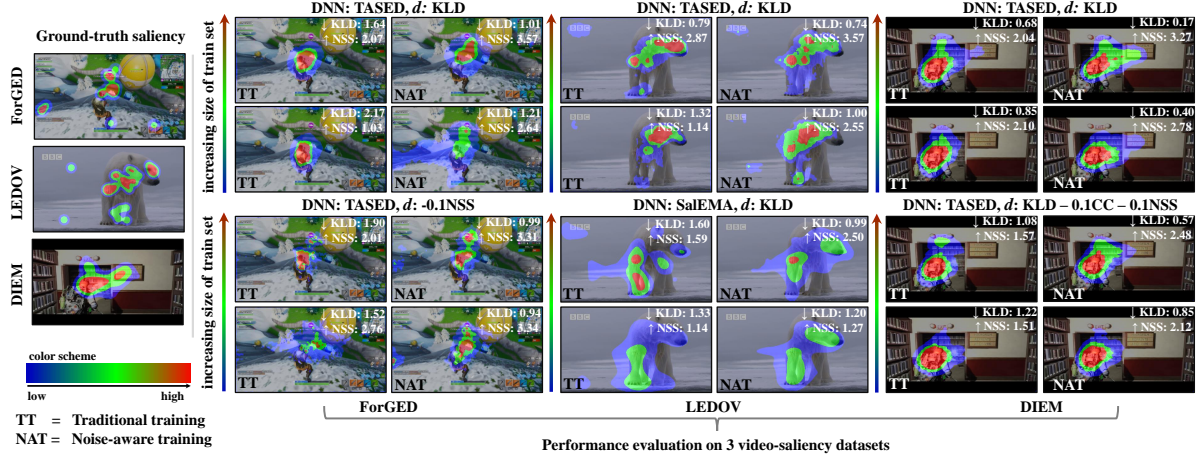


Figure 1: We propose a Noise-Aware Training (NAT) paradigm for video-saliency prediction to address the problem of noise in the training gaze data, which arises out of inaccurate or incomplete human-gaze capture process. We demonstrate the consistent advantage of NAT compared to traditional training (TT) across different DNN architectures (e.g., TASED [40], SalEMA [37]), on different datasets (e.g., our newly introduced ForGED, LEDOV [26], DIEM [41]) and, using different discrepancy functions (KLD, NSS, a mix of KLD, NSS and CC). Here we show some visual examples. The leftmost images show example frames from each dataset we evaluate NAT on, with an overlay of the saliency maps captured using human gaze data (color scheme shown at the bottom left). Each 2×2 array of images on the right shows specific experiments, where we vary the DNN architectures, discrepancy functions, and datasets used for training. The training method (TT or NAT) is mentioned at the bottom, and the performance metrics (KLD, NSS) are reported at the top of each image. Within each 2×2 subset of images, the amount of training data is increased when moving from the bottom to the top row. As is evident, NAT is especially advantageous in cases when less training gaze data is available. *ForGED images have been published with the written permission of Epic Games.*

ing. Therefore, NAT provides a promising approach to effectively train saliency predictors with limited data.

We further notice that existing video-saliency datasets, typically based on natural scenes, often consist of mostly-static content, for which even image-saliency prediction methods can provide a good result [47]. Consequently, assessing how video saliency prediction methods would fare on aspects specific to *videos*, such as temporally-evolving content, is difficult. Therefore we also introduce the Fortnite Gaze Estimation Dataset (ForGED), a video-saliency dataset containing clips obtained from game-play videos of Fortnite, a third-person-shooter game amassing hundreds of million of players worldwide. With ForGED, we contribute a novel dataset with unique characteristics such as: fast temporal dynamics, semantically-evolving content, multiple attractors of attention, and gaming context.

2. Related work

Saliency prediction methods. From the early works that looked at low-level color, intensity, or orientation features to compute saliency maps [24, 23, 31], the field of visual saliency prediction for images has witnessed significant advancement over the past decades. DL approaches have accelerated this progress. Popular existing methods explore combination of learnt features and pre-trained DNNs

at multiple scales [22, 36, 33], generative adversarial networks [42], encoder-decoder architectures [49, 25], dilated convolutions [32], and recurrent networks [38].

Despite the advances in visual saliency for images [8], video saliency prediction remains more challenging because of issues with capturing gaze data (Section 1), and the complexity of the gaze behavior for videos. Existing video-saliency methods are based on architectures such as: (i) 3D CNNs that observe a short sub-sequence of frames [6, 40]; (ii) architectures that leverage temporal aggregation or memory such as LSTMs [37, 50, 18, 52]; or (iii) a combination of both [5]. TASED [40], a 2019 state-of-the-art method on DHF1K [50], belongs to the first class: it uses a 3D CNN encoder-decoder, where the decoder combines temporal features to estimate the saliency. To address the scarcity of training data, the encoder is pre-trained using action recognition as an auxiliary task [53]. SalEMA [37] (also state-of-the-art in 2019) belongs to the second class: it uses an encoder-decoder and deploys temporal aggregation for memory by combining features from previous frames and the current one. The overarching aim with these approaches is to leverage spatial and temporal information from videos. For both categories, some methods also hand-code input features that inform spatial and temporal saliency, such as “object-ness” and motion in a frame [26],

or spatio-temporal feature combination [4]. Other methods combine image and video saliency prediction into a single framework to enable training with a variety of data [14]. For an in-depth discussion of existing saliency methods, we refer the readers to a recent survey [8]. None of these existing methods explicitly account for noise in the training data.

Saliency metrics for training with noisy gaze data. Typically, saliency-prediction algorithms are trained using density-based metrics (such as the Kullback-Leibler Divergence KLD, correlation coefficient CC, SIM [46]), fixation-based metrics (such as NSS [43], AUC [11, 10]), or a combination of these [14, 53]. Fixation-based metrics, by definition, do not require the entire measured saliency map to evaluate the quality of predicted saliency [35]. However, when very few fixation locations are available on a small training dataset, we observe that training with both kinds of metrics show poor performance.

A number of methods tried to account for measurement noise and incomplete sampling when computing statistics on a population [12, 21]. Their key insight is to compensate for the noise by introducing correction terms to the population’s statistics. Attempts to adapt these concepts to gaze data (e.g., when estimating KLD) have been done only at very low spatial resolution [51]: when working at reasonable resolutions for saliency prediction, gaze data tends to be too sparse to collect sufficient statistics in each histogram bin, a prerequisite for the application of these aforementioned methods. This limits the applicability of such methods for designing noise-robust training procedures. In contrast, NAT can be used to train for video saliency in the presence of noise at any resolution.

Video-Saliency Datasets. The progress of deep learning video saliency methods would not be possible without the introduction of large training datasets. Some of these target specific classes of videos (e.g., movies [48], sports [44], faces [39]), while others (like DHF1K [50], LEDOV [26], and DIEM [41]) capture natural visual content [8], and are often used as benchmarks. Among these, DHF1K, a well-known, public dataset, contains inconsistencies that make it difficult to access per-subject gaze data (a requirement to test saliency methods with limited data), and is reported to contain artifacts [47], thus we do not consider it. However, DHF1K is comparable in scope to the LEDOV and DIEM datasets (see Table 1), on which we perform extensive evaluation. For these datasets, a large portion of the video saliency information can be learned effectively by static image-based saliency models [47]. We posit that the fast-changing imagery of a videogame offers a richer source of video-specific saliency problems, including the large and continuous motion of the camera. The only existing saliency dataset for videogames is the Atari-Head dataset [54]. However it does not capture *video* saliency, but

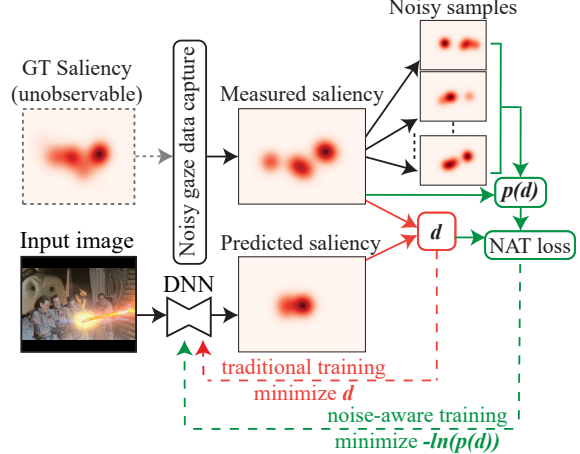


Figure 2: NAT vs. traditional training for saliency prediction. A measured saliency map (obtained using gaze recordings) typically captures a noisy version of the true, unobservable ground-truth (GT) saliency. Traditional deep-learning methods train a deep neural network (DNN) to minimize a discrepancy function d between the measured and predicted saliency maps, which can lead to noise overfitting, especially when little gaze data is available. With our proposed NAT, we estimate the distribution of d to quantify inaccuracies in measured saliency and optimize the DNN for likelihood of d .

fixations on still frames in a sequence. Furthermore, visual features and actions in an Atari game are elementary. This is in contrast with ForGED, the dataset we introduce. ForGED presents gaze data over long and highly dynamic sequences of a first person videogame. A task-specific video-saliency dataset is the Dr(eye)VE dataset — which captures the gaze of the driver in a car [2]. It is an extreme case in which capturing more than one observer per frame is simply not possible. The existence of tasks for which very limited gaze data can be captured further motivate the need to account for measurement noise and incomplete sampling.

3. Noise-Aware Training (NAT)

Let x_i be the probability density function that denotes the i -th, noise-free, ground truth saliency map in a training set. We can train a saliency estimator by minimizing

$$J^{\text{ideal}} = \sum_i d(\hat{x}_i, x_i), \quad (1)$$

where \hat{x}_i is the i -th predicted map, and $d(\cdot, \cdot)$ a discrepancy measure such as KLD, the correlation coefficient CC, NSS, AUC, or a mix of these. In practice, x_i is not available and existing methods minimize

$$J^{\text{real}} = \sum_i d(\hat{x}_i, \tilde{x}_i), \quad (2)$$

where \tilde{x}_i is obtained by combining a limited number of measured gaze fixations. It is therefore an approximation

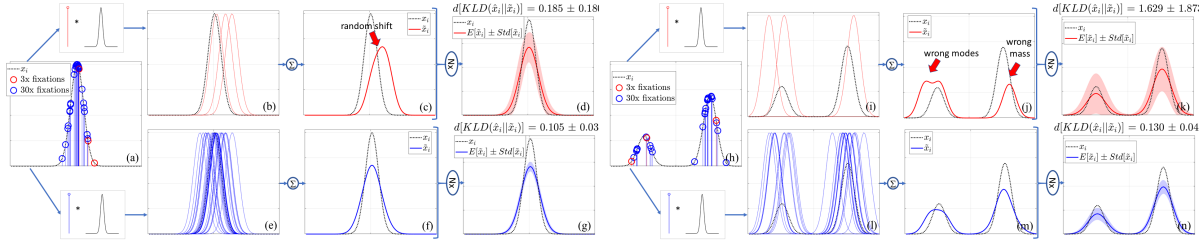


Figure 3: A toy example to motivate NAT. Saliency maps in training datasets are built by first sampling “fixations” (red / blue circles in (a, h)) from the ground truth map (dashed black curves in a, h), then blurring (b, e, i, l), summing, and normalizing to obtain the resulting curves (d, g, j, m). When a limited number of observers is available (e.g., 3, in red), the resulting training map \tilde{x}_i may be shifted or differ in shape from the ground truth x_i . Even when using a high number of fixations (e.g., 50, in blue), the expected \tilde{x}_i differs from x_i because of the blurring. Panels d, g, k, n show the expected value and standard deviation for \tilde{x}_i , compared to x_i . Because of this discrepancy, the statistics $\mathbb{E}[\text{KLD}(x_i, \tilde{x}_i)]$ and $\text{Var}[\text{KLD}(x_i, \tilde{x}_i)]$ are non-zero, and they are larger when few observers are available and also when x_i has a complex shape (e.g., multimodal), which makes x_i more susceptible to inaccurate approximation using \tilde{x}_i . The curves considered here are: a Gaussian centered at $\mu = 50$, $\sigma = 5$; and a mixture with two components at $\mu = [25, 75]$, probabilities $P = [0.3, 0.7]$, and $\sigma = 5$.

of the unobservable x_i , affected by measurement noise and incomplete sampling.

We show that minimizing J^{real} with limited training data may lead to noise overfitting. To address this issue, we introduce the first method to:

- (i) quantify the effect of measurement noise and incomplete sampling in \tilde{x}_i ,
- (ii) propagate the noise from \tilde{x}_i to $d(x_i, \tilde{x}_i)$ and approximate its statistical distribution, $p[d(x_i, \tilde{x}_i)]$, and
- (iii) train a saliency estimator by maximizing $p[d(\hat{x}_i, \tilde{x}_i)]$.

We interpret $d(x_i, \tilde{x}_i)$ as a random variable whose probability density function, $p(d(x_i, \tilde{x}_i))$, depends on the shape of the map and the number of observers in \tilde{x}_i , and it is, therefore, *different for each frame*. We reduce the problem of training a saliency estimator to the minimization of the negative log likelihood:

$$J_{\text{NAT}} = -\ln \prod_i p[d(\hat{x}_i, \tilde{x}_i)] = -\sum_i \ln\{p[d(\hat{x}_i, \tilde{x}_i)]\}, \quad (3)$$

which, as demonstrated experimentally, leads to increased robustness against noise overfitting. Fig. 2 provides a visual comparison of the technical differences between traditional training and NAT.

A toy example. Assume that a method predicts the (unobservable) distribution exactly, that is $\hat{x}_i = x_i$. Because of measurement noise and incomplete sampling in \tilde{x}_i , $d(x_i, \tilde{x}_i) \neq 0$, even though the prediction is perfect. We analyze this in a 1D toy example: Figs. 3(a,h) show two 1D ground-truth saliency maps x_i , one unimodal, and one bimodal. We simulate gaze-data acquisition by sampling 3 (red circles) or 30 (blue) “fixations” from x_i . The random positions of the fixations mimic the measurement noise,

while their finite number simulates incomplete sampling. Following the *de facto* standard to generate saliency maps from single gaze locations, we blur each fixation (Fig. 3(b)), and combine the resulting curves (Fig. 3(c)).

When few fixations are available, \tilde{x}_i may be shifted with respect to x_i (Fig. 3(c)), and the number of its modes may not match x_i (Fig. 3(j)). Furthermore, when x_i is multimodal, the mass of each mode in \tilde{x}_i may be imprecisely estimated compared to x_i (Fig. 3(j)). To demonstrate the point (i) enlisted earlier, we collect 1,000 random realizations of \tilde{x}_i and show that the uncertainty on \tilde{x}_i , measured by $\text{Std}[\tilde{x}_i]$, decreases for a large number of fixations (Figs. 3(d, k) vs. Figs. 3(g, n)). However, $\mathbb{E}[\tilde{x}_i]$ still differs from x_i because of the blurring operation.

Having defined the map generation process, and shown the effect of measurement and sampling noise on \tilde{x}_i , we can estimate the distribution $p[d(x_i, \tilde{x}_i)]$ (to show point (ii)). The analytical expression for $p[d(x_i, \tilde{x}_i)]$ depends on the discrepancy function d and it is impractical or unfeasible to derive, so we settle for computing $\text{KLD}(x_i, \tilde{x}_i)$ in 1,000 random realizations of \tilde{x}_i and get $\mathbb{E}[\text{KLD}(x_i, \tilde{x}_i)]$, $\text{Std}[\text{KLD}(x_i, \tilde{x}_i)]$. These are reported in Figs. 3(d, g, k, n). We use KLD as discrepancy function because of its wide adoption for saliency estimation, but the results presented here hold for other metrics as well. We observe that:

- $\mathbb{E}[\text{KLD}(x_i, \tilde{x}_i)] > 0$, *i.e.* $\text{KLD}(x_i, \tilde{x}_i)$ is biased. The source of the bias is twofold. First, $\text{KLD}(x_i, \tilde{x}_i) > 0$ because $\mathbb{E}[\tilde{x}_i]$ is a smoothed version of x_i , independently from the number of observers. Second, \tilde{x}_i is noisy ($\text{Std}[\tilde{x}_i] > 0$), which, especially for a limited number of observers, contributes with an additional positive term to $\text{KLD}(x_i, \tilde{x}_i)$.
- $\text{Std}[\text{KLD}(x_i, \tilde{x}_i)] > 0$, and it tends to be smaller for a larger number of observers.

- For a given number of observers, $\mathbb{E}[\text{KLD}(x_i, \tilde{x}_i)]$ and $\text{Std}[\text{KLD}(x_i, \tilde{x}_i)]$ are larger for multimodal maps.

We conclude that, when \tilde{x}_i is affected by measurement noise and incomplete sampling, the expected value and variance of the discrepancy $d(x_i, \tilde{x}_i)$ are not zero, depend on the number of observers, and are different for each frame. These properties, which also hold for 2D saliency maps recorded from real human observers, form the basis for the development and interpretation of NAT.

The noise-aware training (NAT) procedure. NAT modifies the traditional training cost function in Eq. 2 to take into account the presence of noise in the training data; it can be applied to different discrepancy measures d . NAT is inspired by discrepancy principles proposed in other contexts, like image denoising [7, 16], and based on the idea that \hat{x}_i should not perfectly match the noisy \tilde{x}_i , as this may lead to noise overfitting. Instead of minimizing J^{real} in Eq. 2, we assume that $d(x_i, \tilde{x}_i)$ follows a Gaussian distribution. After solving for the logarithm and removing the constant terms in Eq. 3 (see Supplementary), we have:

$$J_{\text{NAT}}^{\text{ideal}} = \sum_i \frac{[d(\hat{x}_i, \tilde{x}_i) - \mathbb{E}[d(x_i, \tilde{x}_i)]]^2}{\text{Var}[d(x_i, \tilde{x}_i)]}. \quad (4)$$

Like traditional cost functions, $J_{\text{NAT}}^{\text{ideal}}$ penalizes predicted \hat{x}_i that lie too far from \tilde{x}_i . However, it also introduces the idea that estimates should not be *too close* to \tilde{x}_i , which helps prevent overfitting. Furthermore, the penalization is inversely proportional to the variance of $d(x_i, \tilde{x}_i)$, *i.e.* it is strong only for those frames whose discrepancy can be accurately measured. In practice, since $\mathbb{E}[d(x_i, \tilde{x}_i)]$ and $\text{Var}[d(x_i, \tilde{x}_i)]$ are large for multimodal, sparse maps with few fixations (as seen in the toy example), NAT strongly penalizes errors in \hat{x}_i for focused, unimodal saliency maps with many observers. On the other hand, it weakly penalizes the errors in \hat{x}_i for widespread sparse gaze maps with few observers in \tilde{x}_i , which are considered unreliable for training.

Eq. 4 cannot be implemented in practice, as the ground truth x_i is unknown. All we have access to is \tilde{x}_i , a noisy realization of x_i . We therefore approximate the statistics of $d(x_i, \tilde{x}_i)$ as follows:

$$\mathbb{E}[d(x_i, \tilde{x}_i)] \approx \mathbb{E}[d(\tilde{x}_i, \tilde{x}_i)], \quad (5)$$

$$\text{Var}[d(x_i, \tilde{x}_i)] \approx \text{Var}[d(\tilde{x}_i, \tilde{x}_i)], \quad (6)$$

where \tilde{x}_i is the map obtained by sampling and combining fixations from \tilde{x}_i instead of x_i . Intuitively, we use the spatial noise introduced by sampling from \tilde{x}_i as a proxy of the non-ideality introduced by the gaze-capturing process. Eqs. 5 and 6 are our best option, but they still introduce an approximation. However, we observe empirically that these approximations hold (see Supplementary for a detailed analysis), which is the reason why NAT outperforms

traditional training, as we show in Sec. 5. We resort to sample estimation to compute $\mathbb{E}[d(\tilde{x}_i, \tilde{x}_i)]$ and $\text{Var}[d(\tilde{x}_i, \tilde{x}_i)]$: for any frame, we sample the prescribed number of observers from \tilde{x}_i to generate multiple \tilde{x}_i and compute the sample mean $\widetilde{\mathbb{E}}[d(\tilde{x}_i, \tilde{x}_i)]$ and variance $\widetilde{\text{Var}}[d(\tilde{x}_i, \tilde{x}_i)]$ of $d(\tilde{x}_i, \tilde{x}_i)$. The application of the NAT paradigm for training reduces then to the minimization of:

$$J_{\text{NAT}}^{\text{real}} = \sum_i \frac{[d(\hat{x}_i, \tilde{x}_i) - \widetilde{\mathbb{E}}[d(\tilde{x}_i, \tilde{x}_i)]]^2}{\widetilde{\text{Var}}[d(\tilde{x}_i, \tilde{x}_i)]}, \quad (7)$$

where all the terms are now well-defined. Any DNN can be trained through NAT using the cost function in Eq. 7.

4. The ForGED dataset

When compared to natural videos in LEDOV and DIEM, videogames represent an interesting, diverse, and challenging application area for saliency methods. It is interesting, because of the large market value. It is diverse and challenging, because of the varying visual appearance, the fast temporal dynamics, the plurality of the objects of interest in a scene, and dependence of human gaze on temporal semantics — something that is missing in many natural-scene videos datasets [47]. For these reasons we introduce ForGED, a dataset with gaze data for video clips of Fortnite, a third-person shooter videogame counting hundreds of millions of players worldwide, and even more YouTube followers.

The gaze acquisition process was twofold. The first phase was game-play video recording: 8 players (7 amateurs, 1 professional) volunteered to play in Fortnite Battle Royale mode, season 9 and 10, for a total of 12 hours of videos collected through OBS [1]. In the second phase (spectator recording) we split the game-play videos into 480 clips, each 15s long, and shuffled them in random sequences of 48 clips each. The game-play clips were separated by a 3s interval with a central red dot on a grey screen, with the aim of having a consistent gaze starting point during each game-play clip. 102 volunteers, approximately half of which familiar with Fortnite, observed the sequences, sitting at approximately 80cm from the display, wearing headsets for the game sounds, while we collected their gaze using a Tobii Tracker4C at 90Hz. Each session lasted less than 15 mins, to avoid fatigue. 5 – 21 observers were captured for each clip (see Table 1). After analyzing the typical gaze patterns, we discarded the initial two seconds of each clip, when observers were mostly spending time to understand the context, to get a total of 374,400 video frames with reliable gaze data. The 380 training clips contain 5 observers per frame, while the validation (25) and testing (75) clips have 15 to 21 observers to reduce the effect of noise.¹ The

¹Although we collected players' gaze data as well, we excluded them from further processing, as game playing and spectating are different visual tasks that generate different fixation patterns.

Dataset	Videos	Frames	Resolution	Max. Obs. for training	Obs. for testing	Content type
DIEM [41]	60	240,015	720p@30Hz	31	51-219	everyday videos (trailers, advs, ...)
LEDOV [26]	538	179,336	720p@24Hz	32	32	human/animal activities
ForGED (ours)	480	374,400	1080p@60hz	5 - 15	15-21	videogame (Fortnite)

Table 1: Characteristics of video-saliency datasets, including the proposed ForGED dataset. We report the maximum-available observers in the training set for each dataset and the total observers available in test sets.

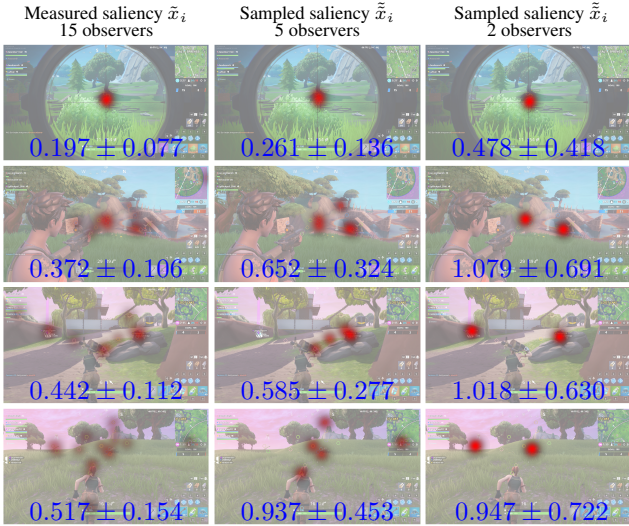


Figure 4: Typical frames from ForGED. The first column shows the measured 15-observers saliency map \tilde{x}_i in red; the second and third columns show sampled \tilde{x}_i maps with 5 and 2 observers respectively. We report in each panel the corresponding $\widetilde{\mathbb{E}}[\text{KLD}(\tilde{x}_i \parallel \tilde{x}_i)] \pm \text{Std}[\text{KLD}(\tilde{x}_i \parallel \tilde{x}_i)]$. As shown here, these quantities increase when the saliency map becomes sparse, and the number of observers shrinks, making frames less reliable for training. *ForGED images have been published with the written permission of Epic Games.*

main characteristics of ForGED are reported in Table 1.

Fig. 4 show typical ForGED testing frames. Some measured 15-observer saliency maps \tilde{x}_i are overlaid in red in the first column: they present a large variety. Some are unimodal: in the first row, the player is aiming at an enemy; the estimated bias $\widetilde{\mathbb{E}}[\text{KLD}(\tilde{x}_i \parallel \tilde{x}_i)]$ and standard deviation $\widetilde{\text{Std}}[\text{KLD}(\tilde{x}_i \parallel \tilde{x}_i)]$ are small, and they slightly grow if the number of observers shrinks (second and third columns). This kind of frame is considered highly informative in NAT. Other saliency maps are bi- or tri-modal. In the second row, the human attention is mostly on other characters and the top-right mini-map; in the third row, the observers are focused on text and the main character. When compared to the first row, these frames have larger bias and standard deviation on KLD, because of the sparsity of the fixations. In the last row, the character is running in an uninteresting scenario: consequently, the fixation map is exploratory, with random locations covered by the observers. The sparse fixation density of such saliency maps is associated with higher

levels of bias and standard deviation in KLD, that render such frames less reliable according to the NAT paradigm.

5. Results

To compare NAT (Eq. 7) and traditional training (Eq. 2), we experiment with: 1) varying number of training videos and observers on ForGED and two existing datasets (LEDOV [26], and DIEM [41]); 2) adopting density-based or fixation-based discrepancy functions; and 3) two different DNN architectures. We report an entire set of saliency metrics (KLD, CC, SIM, NSS, and AUC-J) to make the evaluation complete, as every metric penalizes artifacts differently [11, 35]. To limit the effect of noise in evaluation, we use test sets that contain saliency maps from a *larger* number of observers when compared to training (Table 1). Both training and testing saliency maps are obtained by the widely-used practice of blurring binary fixation maps with a Gaussian kernel of size $\sim 1^\circ$ viewing angle. We discuss alternative strategies as well [33, 36, 35].

videos	obs.	train	KLD \downarrow	CC \uparrow	SIM \uparrow	NSS \uparrow	AUC-J \uparrow
30	2	Eq. (2)	1.385	0.546	0.370	2.992	0.877
		NAT	1.298	0.558	0.385	3.161	0.903
	5	Eq. (2)	1.419	0.536	0.370	3.042	0.877
100	15	Eq. (2)	1.080	0.615	0.481	3.598	0.897
		NAT	0.995	0.634	0.478	3.750	0.924
	2	Eq. (2)	1.323	0.565	0.365	3.034	0.890
379	5	Eq. (2)	1.065	0.623	0.473	3.627	0.917
		NAT	0.969	0.643	0.494	3.749	0.923
	2	Eq. (2)	0.986	0.628	0.475	3.434	0.925
		NAT	0.974	0.632	0.470	3.497	0.932
	5	Eq. (2)	0.963	0.631	0.461	3.376	0.936
		NAT	0.888	0.664	0.508	3.813	0.934

Table 2: NAT vs. traditional training on ForGED for TASED, $d = \text{KLD}$, various number of training videos and observers. Best metrics for each pair of experiments in bold.

5.1. Dataset type and size

We first compare NAT (Eq. 7) and traditional training (Eq. 2) on all three datasets using a variable number of training videos and observers per video. We adopt the 3D-CNN-based TASED architecture [40] and the prescribed hyper-parameters ($d = \text{KLD}$; action-recognition pretraining) with one exception: we use RMSprop [20], since it provides better results for traditional training (see Supplementary). Table 2 shows the results on ForGED, when using 30, 100, or 379 training videos, and 2, 5, or 15 observers. NAT consistently outperforms traditional training when the number of training videos is ≤ 100 , *i.e.*, when the effect of noise

videos	obs.	train	KLD \downarrow	CC \uparrow	SIM \uparrow	NSS \uparrow	AUC-J \uparrow
30	2	Eq. (2)	2.155	0.195	0.198	1.007	0.793
	5	Eq. (2)	1.744	0.371	0.265	1.763	0.861
	30	Eq. (2)	1.431	0.428	0.378	2.082	0.884
100	2	NAT	1.189	0.495	0.409	2.378	0.902
	5	NAT	1.098	0.554	0.443	2.753	0.902
	30	NAT	1.120	0.532	0.433	2.638	0.909
461	2	Eq. (2)	1.882	0.315	0.275	1.621	0.787
	5	NAT	1.449	0.457	0.367	2.281	0.869
	30	Eq. (2)	1.351	0.460	0.382	2.331	0.890
2, 5, 15, 30	2	NAT	1.170	0.524	0.424	2.687	0.904
	5	NAT	0.872	0.648	0.493	3.604	0.932
	15	Eq. (2)	1.231	0.532	0.459	2.784	0.880
	30	NAT	0.975	0.595	0.499	2.931	0.921
	2, 5, 15, 30	NAT	0.828	0.667	0.531	3.530	0.929

Table 3: NAT vs. traditional training on LEDOV for TASED, $d = \text{KLD}$, various number of training videos and observers. The last two rows show the case of an unbalanced dataset having frames with 2, 5, 15, or 30 observers. Best metrics for each pair of experiments in bold.

is large or overfitting may occur. The gap between NAT and traditional training tends to shrink when using the entire dataset, which makes overfitting less likely. NAT on 30 videos / 15 observers and on 100 videos / 5 observers is comparable or superior to traditional training with 379 videos / 5 observers, roughly corresponding to at least a $3\times$ saving factor in terms of data required for training. Similar conclusions can be drawn when training with the LEDOV (Table 3) and DIEM (see Supplementary) datasets.

We also test an interesting case of practical importance where, for any reason, an *unbalanced* training dataset is available, with uneven number of observers in the training videos. In this case, NAT accounts for the varying reliability of the gaze data in training frames. The last two rows of Table 3 report metrics for TASED trained on the unbalanced LEDOV dataset and we note significantly better quality metrics with NAT compared to traditional training.

5.2. Discrepancy functions

NAT can be applied to any training discrepancy d beyond the case of the density-based discrepancy KLD tested in Sec. 5.1. To demonstrate this, we train TASED on ForGED with traditional training and NAT using: 1) the fixation-based discrepancy $d = -0.1\text{NSS}$ (Table 4); and 2) a mix of density-based and fixation-based discrepancies, $d = \text{KLD} - 0.1\text{CC} - 0.1\text{NSS}$, which has been a popular choice in literature [14, 50] (Table 5). In these experiments, NAT again achieves better metrics than traditional training (with one exception discussed below), independently of the training discrepancy metric being optimized. The advantage is more evident for a limited number of observers and videos, while the gap between traditional training and NAT tends to reduce when using the full dataset. Similar results for the LEDOV and DIEM datasets, TASED and an additional DNN architecture are reported in the Supplementary

and further demonstrate the generality of these conclusions.

In Table 4, we notice that NAT overcomes traditional training in terms of NSS only for 2 or 5 observers, and 30 training videos. Recall that, by design, NSS optimizes the predicted saliency map only at the measured fixation locations. Consequently, when few fixations per frame are available for training, a high NSS score may not generalize well to other evaluation metrics that evaluate different aspects of the quality of a predicted saliency map. This can be alleviated by additional regularization (such as using additional metrics as we do with $d = \text{KLD} - 0.1\text{CC} - 0.1\text{NSS}$ in Table 5 and observe that high NSS scores generalize to good performance in terms of other metrics). In other words, for few-observer training, optimizing for NSS alone may not constrain the predicted saliency map sufficiently — which shows up as poor generalization to other metrics. This is what we observe in Table 4, where the regularizing effect of NAT leads to worse NSS values compared to traditional training; but, *all* of the other evaluation metrics indicate NAT to be better.

videos	obs.	train	KLD \downarrow	CC \uparrow	SIM \uparrow	NSS \uparrow	AUC-J \uparrow
30	2	Eq. (2)	2.005	0.362	0.302	2.677	0.788
	5	NAT	1.408	0.528	0.371	3.163	0.887
	15	Eq. (2)	1.642	0.489	0.28	3.212	0.898
100	2	NAT	1.254	0.566	0.417	3.39	0.906
	5	Eq. (2)	1.518	0.506	0.403	3.672	0.826
	30	NAT	1.155	0.608	0.435	3.552	0.91
379	2	Eq. (2)	1.328	0.563	0.383	3.783	0.899
	5	NAT	1.206	0.584	0.426	3.44	0.906
	30	Eq. (2)	1.312	0.578	0.452	3.983	0.835
379	2	NAT	1.165	0.61	0.475	3.747	0.879
	5	Eq. (2)	1.163	0.614	0.475	4.161	0.857
	30	NAT	1.028	0.642	0.495	3.858	0.901

Table 4: NAT vs. traditional training (TT) on ForGED for TASED, $d = -0.1\text{NSS}$ (a fixation-based discrepancy), various number of training videos and observers. Best metrics for each pair of experiments in bold.

videos	obs.	train	KLD \downarrow	CC \uparrow	SIM \uparrow	NSS \uparrow	AUC-J \uparrow
30	2*	Eq. (2)*	1.523	0.526	0.324	3.016	0.874
	5	NAT*	1.375	0.558	0.347	3.048	0.895
	15	Eq. (2)	1.095	0.612	0.440	3.600	0.904
100	2	NAT	1.061	0.618	0.466	3.656	0.912
	5	Eq. (2)	1.097	0.623	0.425	3.533	0.919
	30	NAT	0.993	0.639	0.475	3.802	0.928
379	2	Eq. (2)	1.138	0.601	0.429	3.406	0.911
	5	NAT	1.099	0.600	0.434	3.356	0.920
	30	Eq. (2)	1.016	0.631	0.468	3.644	0.924
379	2	NAT	1.011	0.626	0.450	3.459	0.931
	5	Eq. (2)	0.958	0.655	0.467	3.652	0.934
	30	NAT	0.905	0.669	0.496	3.946	0.933

Table 5: NAT vs. traditional training on ForGED for TASED, $d = \text{KLD} - 0.1\text{CC} - 0.1\text{NSS}$, various number of training videos and observers. Due to training instability, for 30 videos / 2 observers we use $d = \text{KLD} - 0.1\text{CC}$. Best metrics for each pair of experiments in bold.

videos	obs.	train	KLD↓	CC↑	SIM↑	NSS↑	AUC-J↑
30	2	Eq. (2)	1.922	0.249	0.232	1.039	0.803
		NAT	1.768	0.286	0.285	1.263	0.843
	5	Eq. (2)	2.168	0.280	0.276	1.348	0.844
		NAT	1.710	0.327	0.298	1.476	0.848
	30	Eq. (2)	1.888	0.256	0.225	1.082	0.821
		NAT	1.510	0.404	0.321	1.969	0.874
100	2	Eq. (2)	1.621	0.355	0.307	1.634	0.854
		NAT	1.538	0.385	0.311	1.733	0.867
	5	Eq. (2)	1.381	0.455	0.363	2.179	0.882
		NAT	1.340	0.470	0.392	2.368	0.893
	30	Eq. (2)	1.359	0.532	0.408	2.909	0.883
		NAT	1.284	0.559	0.408	3.272	0.884
461	2	Eq. (2)	1.277	0.487	0.382	2.247	0.895
		NAT	1.243	0.490	0.403	2.365	0.899
	5	Eq. (2)	1.139	0.568	0.444	2.825	0.903
		NAT	1.136	0.567	0.450	3.117	0.908
	30	Eq. (2)	1.052	0.612	0.462	3.237	0.912
		NAT	1.045	0.633	0.457	3.425	0.910

Table 6: NAT vs. traditional training on LEDOV for SalEMA, $d = \text{KLD}$, various number of training videos and observers. Best metrics for each pair of experiments in bold.

5.3. DNN architectures

Next, we show that NAT applies to DNN architectures other than TASED by training SalEMA [37] on LEDOV and ForGED. Table 6 shows that NAT outperforms traditional training and the gap shrinks for large number of training videos. The Supplementary shows more results.

5.4. Discussion

NAT for images. Image-based saliency datasets (e.g., CAT2000 [9], SALICON [27]) typically have many fixations per image. Measurement noise and incomplete sampling are less of a concern with such datasets, as increasing the number of fixations rapidly generates fairly accurate ground-truth maps (e.g., $> 90\%$ accuracy at 20 fixations [28]). It is however fair to ask if one can apply NAT to the case of images, to train with less data even in this case. To answer this question, we simulate a high-noise, incomplete, image dataset by sampling a subset of the total available fixations (which are at minimum 139) for each image in SALICON². Then we train EML-Net [25], using the hyperparameters, EML discrepancy, and training procedure as proposed by the authors (see Supplementary) with traditional training and NAT, and evaluate it on the test set of the official SALICON benchmark. Table 7, shows the results for varying number of fixations, and confirms the advantage of NAT over traditional training also in the case of images.

Alternative methods to estimate \tilde{x} . Estimating \tilde{x} using a Gaussian-blur kernel is prevalent practice in video-saliency research, but more principled strategies that promise to automatically handle data noise and sparsity also exist, e.g., based on Kernel Density Estimation (KDE). For instance, the saliency map, \tilde{x} , can be estimated from the measured

fixations	train	KLD↓	CC↑	SIM↑	NSS↑	AUC-J↑
5	Eq. (2)	3.986	0.578	0.537	1.477	0.764
	NAT	1.672	0.660	0.611	1.549	0.817
15	Eq. (2)	2.877	0.655	0.589	1.669	0.795
	NAT	1.437	0.714	0.640	1.676	0.831

Table 7: Performance of EML-Net, trained with traditional training and NAT on the SALICON training set with a reduced number of fixations. Results shown on the full SALICON test set.

fixations using Gaussian kernel functions in KDE with a uniform regularization, where the optimal KDE bandwidth and the weight of the uniform regularization term are set to maximize a gold-standard model for saliency prediction [34, 47]. We adopt this approach as an alternative method to estimate \tilde{x} .

We find similarities between KDE and NAT: KDE captures the gaze uncertainty by generating a smooth, almost-uniform map for frames with few, sparse gaze locations. NAT gives small importance to such frames in training, and allows \tilde{x}_i to deviate from the training saliency map according to the expected statistical distribution. Thus we believe it is important to ask if processing fixations through KDE, instead of taking noise into account in the cost function as in NAT, is equivalently effective. Table 8 compares traditional training with a fixed-size blur, KDE target saliency maps [47], and NAT for ForGED, 5 observers, 30 videos. While estimating the training saliency maps with KDE instead of fixed-size blur led to an improvement in the metrics, NAT still yields the best results.

\tilde{x}_i for training	training	KLD↓	CC↑	SIM↑	NSS↑	AUC-J↑
1° blur	Eq. (2)	1.419	0.536	0.370	3.042	0.877
	KDE	1.223	0.573	0.399	3.271	0.897
	NAT	1.172	0.590	0.428	3.372	0.908

Table 8: Comparing different strategies for estimating \tilde{x} for traditional training. While KDE-estimated \tilde{x} for training yields an improvement over fixed-size blurring, NAT still outperforms the traditional training approach. Training dataset: ForGED, 5 observers, 30 videos.

Limitations and future work. We base the practical derivation of NAT on two main approximations: 1) we assume that $d(x_i, \tilde{x}_i)$ has a Gaussian distribution, and 2) we sample from \tilde{x}_i (instead of x_i) in Eqs. 5-6. For the first approximation, we note that although $d(x_i, \tilde{x}_i)$ is typically strictly positive (e.g., in the case of KLD) and its distribution is consequently asymmetric, we observe that most often, $\mathbb{E}[d(\tilde{x}_i || \tilde{x}_i)] \geq 2 \cdot \mathbb{S}td[d(\tilde{x}_i || \tilde{x}_i)]$ (e.g., see Fig. 4). This makes our approximation a good first guess for modeling the distribution of $d(x_i, \tilde{x}_i)$. We expect better models would further improve NAT. As for our second approximation (Eqs. 5-6), where we sample from \tilde{x}_i instead of x_i , we report a detailed analysis of the level of accuracy in the Supplementary. The intuition is that, if x_i and \tilde{x}_i have a similar

²Mouse clicks are used as proxy for gaze in SALICON.

shape (e.g., see Fig. 2), the approximation $\mathbb{E}[d(x_i||\tilde{x}_i)] \approx \widetilde{\mathbb{E}}[d(\tilde{x}_i||\tilde{x}_i)]$ and $\text{Var}[d(x_i||\tilde{x}_i)] \approx \widetilde{\text{Var}}[d(\tilde{x}_i||\tilde{x}_i)]$ can be leveraged.

A second limitation, which is common to video-saliency research, is that, even if test sets are generally derived from a large number of fixations, measurement noise and incomplete sampling can still affect them and add uncertainty about the conclusions one can draw. The problem of evaluating saliency methods has been widely studied for images [11, 35], and a more principled approach, such as deriving metric-specific saliency from the probabilistic output of a saliency predictor, can give a clearer understanding. However, we note that all the metrics in our evaluation are generally in agreement with one another regarding the ranking of the methods, which further provides strong evidence of the advantages provided by NAT over traditional training. A potential direction for future work on evaluating saliency methods can be based on the design principles of NAT, where we give more or less importance to frames in a test set depending on the noise level in these frames.

6. Conclusion

Gaze data acquisition is time consuming, and prone to inaccuracies. To reduce the impact of these limitations on the field of saliency estimation, we introduce a model that quantifies the uncertainty in training data for saliency prediction, and a new dataset for testing our model which is the first to offer a video-game context to the video saliency community. We show that NAT consistently leads to an improvement in the quality of the predicted saliency maps, especially when few videos and observers are available. The adoption of NAT has important practical implications, as it prevents overfitting to noise in gaze data while training saliency models, and therefore allows training with a reduced amount of data, both in terms of videos and number of observers, without loss of quality. Beyond being applied for training, our model can also be extended to encompass the case of evaluation in future.

Acknowledgments

We thank Abhishek Badki and Shoaib Ahmed Siddiqui for help with distributed training, Jan Kautz and Arash Vahdat for technical discussions, Michael Stengel for help with gaze-recording software, Paul Weakliem and Nathan Rogers for UCSB computational infrastructure, and the Fortnite players and observers for their help with creating ForGED. This work was supported in part through computational facilities purchased using NSF grant OAC-1925717 and administered by the Center for Scientific Computing (CSC) at UCSB. The CSC is supported by the California NanoSystems Institute and the Materials Research Science and Engineering Center (MRSEC; NSF DMR 1720256).

References

- [1] Open broadcaster software. <https://obsproject.com/>. 5
- [2] Stefano Alletto, Andrea Palazzi, Francesco Solera, Simone Calderara, and Rita Cucchiara. Dr (eye) ve: a dataset for attention-based tasks with applications to autonomous and assisted driving. In *Proceedings of the ieee conference on computer vision and pattern recognition workshops*, 2016. 3
- [3] Duin Baek, Hangil Kang, and Jihoon Ryoo. Sali360: Design and implementation of saliency based video compression for 360° video streaming. In *Proceedings of the 11th ACM Multimedia Systems Conference*, 2020. 1
- [4] Cagdas Bak, Aysun Kocak, Erkut Erdem, and Aykut Erdem. Spatio-temporal saliency networks for dynamic saliency prediction. *IEEE Transactions on Multimedia*, 2017. 3
- [5] Loris Bazzani, Hugo Larochelle, and Lorenzo Torresani. Recurrent mixture density network for spatiotemporal visual attention. *arXiv*, 2016. 2
- [6] Giovanni Bellitto, Federica Proietto Salanitri, Simone Palazzo, Francesco Rundo, Daniela Giordano, and Concetto Spampinato. Video saliency detection with domain adaption using hierarchical gradient reversal layers. *arXiv*, 2020. 2
- [7] M Bertero, P Boccacci, G Talenti, R Zanella, and L Zanni. A discrepancy principle for poisson data. 2010. 5
- [8] Ali Borji. Saliency prediction in the deep learning era: Successes and limitations. *IEEE Transactions on Pattern Analysis and Machine Intelligence (TPAMI)*, 2019. 2, 3
- [9] Ali Borji and Laurent Itti. Cat2000: A large scale fixation dataset for boosting saliency research. *CVPR 2015 workshop on "Future of Datasets"*, 2015. arXiv preprint arXiv:1505.03581. 8
- [10] Zoya Bylinskii, Tilke Judd, Ali Borji, Laurent Itti, Frédéric Durand, Aude Oliva, and Antonio Torralba. Mit saliency benchmark. 2015. 3
- [11] Zoya Bylinskii, Tilke Judd, Aude Oliva, Antonio Torralba, and Frédéric Durand. What do different evaluation metrics tell us about saliency models? *IEEE Transactions on Pattern Analysis and Machine Intelligence (TPAMI)*, 2018. 3, 6, 9
- [12] Anne Chao and Tsung-Jen Shen. Nonparametric estimation of shannon's index of diversity when there are unseen species in sample. *Environmental and Ecological Statistics*, 2003. 3
- [13] Arturo Deza and Miguel P. Eckstein. Can peripheral representations improve clutter metrics on complex scenes? In *Advances in Neural Information Processing Systems (NeurIPS)*, 2016. 1
- [14] Richard Droste, Jianbo Jiao, and J. Alison Noble. Unified Image and Video Saliency Modeling. In *Proceedings of the European Conference on Computer Vision (ECCV)*, 2020. 3, 7, 13
- [15] Anna Maria Feit, Shane Williams, Arturo Toledo, Ann Paradiso, Harish Kulkarni, Shaun Kane, and Meredith Ringel Morris. Toward everyday gaze input: Accuracy and precision of eye tracking and implications for design. In *Chi conference on human factors in computing systems*, 2017. 1
- [16] I. Frosio and J. Kautz. Statistical nearest neighbors for image denoising. *IEEE Transactions on Image Processing (TIP)*, 2019. 5

[17] Wilson S Geisler and Jeffrey S Perry. Real-time foveated multiresolution system for low-bandwidth video communication. In *Real-time foveated multiresolution system for low-bandwidth video communication*, 1998. 1

[18] Siavash Gorji and James J Clark. Going from image to video saliency: Augmenting image salience with dynamic attentional push. In *Proceedings of the IEEE Conference on Computer Vision and Pattern Recognition (CVPR)*, 2018. 2

[19] Kaiming He, Xiangyu Zhang, Shaoqing Ren, and Jian Sun. Deep residual learning for image recognition. In *Proceedings of the IEEE conference on computer vision and pattern recognition*, pages 770–778, 2016. 15

[20] Geoffrey Hinton, Nitish Srivastava, and Kevin Swersky. Neural networks for machine learning lecture 6a overview of mini-batch gradient descent. 2012. 6

[21] D Holste, I Grosse, and H Herzl. Bayes' estimators of generalized entropies. *Journal of Physics A: Mathematical and General*, 1998. 3

[22] Xun Huang, Chengyao Shen, Xavier Boix, and Qi Zhao. Salicon: Reducing the semantic gap in saliency prediction by adapting deep neural networks. In *Proceedings of the IEEE International Conference on Computer Vision (ICCV)*, 2015. 1, 2

[23] Laurent Itti and Christof Koch. A saliency-based search mechanism for overt and covert shifts of visual attention. *Vision research*, 2000. 1, 2

[24] Laurent Itti, Christof Koch, and Ernst Niebur. A model of saliency-based visual attention for rapid scene analysis. *IEEE Transactions on Pattern Analysis and Machine Intelligence (TPAMI)*, 1998. 1, 2

[25] Sen Jia and Neil DB Bruce. Eml-net: An expandable multi-layer network for saliency prediction. *Image and Vision Computing*, 2020. 1, 2, 8, 15

[26] Lai Jiang, Mai Xu, Tie Liu, Minglang Qiao, and Zulin Wang. DeepVS: A deep learning based video saliency prediction approach. In *Proceedings of the European Conference on Computer Vision (ECCV)*, 2018. 2, 3, 6, 13

[27] Ming Jiang, Shengsheng Huang, Juanyong Duan, and Qi Zhao. Salicon: Saliency in context. In *Proceedings of the IEEE Conference on Computer Vision and Pattern Recognition (CVPR)*, 2015. 8, 15

[28] Tilke Judd, Frédo Durand, and Antonio Torralba. A benchmark of computational models of saliency to predict human fixations. 2012. 8, 12, 13

[29] Anton S. Kaplanyan, Anton Sochenov, Thomas Leimkühler, Mikhail Okuney, Todd Goodall, and Gizem Rufo. Deepfovea: Neural reconstruction for foveated rendering and video compression using learned statistics of natural videos. *ACM Transactions on Graphics (SIGGRAPH)*, 2019. 1

[30] Jonghyun Kim, Youngmo Jeong, Michael Stengel, Kaan Akşit, Rachel Albert, Ben Boudaoud, Trey Greer, Joohwan Kim, Ward Lopes, Zander Majercik, Peter Shirley, Josef Spjut, Morgan McGuire, and David Luebke. Foveated ar: Dynamically-foveated augmented reality display. *siggraph*, 2019. 1

[31] Christof Koch and Shimon Ullman. Shifts in selective visual attention: towards the underlying neural circuitry. In *Matters of intelligence*. 1987. 1, 2

[32] Srinivas SS Kruthiventi, Kumar Ayush, and R Venkatesh Babu. Deepfix: A fully convolutional neural network for predicting human eye fixations. *IEEE Transactions on Image Processing (TIP)*, 2017. 1, 2

[33] Matthias Kümmerer, Lucas Theis, and Matthias Bethge. Deep gaze i: Boosting saliency prediction with feature maps trained on imagenet. *arXiv*, 2014. 1, 2, 6

[34] Matthias Kümmerer, Thomas SA Wallis, and Matthias Bethge. Information-theoretic model comparison unifies saliency metrics. *Proceedings of the National Academy of Sciences*, 2015. 8, 16

[35] Matthias Kümmerer, Thomas SA Wallis, and Matthias Bethge. Saliency benchmarking made easy: Separating models, maps and metrics. In *Proceedings of the European Conference on Computer Vision (ECCV)*, 2018. 3, 6, 9

[36] Matthias Kümmerer, Thomas SA Wallis, Leon A Gatys, and Matthias Bethge. Understanding low-and high-level contributions to fixation prediction. In *Proceedings of the IEEE International Conference on Computer Vision (ICCV)*, 2017. 1, 2, 6

[37] Panagiotis Linardos, Eva Mohedano, Juan Jose Nieto, Noel E O'Connor, Xavier Giro-i Nieto, and Kevin McGuinness. Simple vs complex temporal recurrences for video saliency prediction. 2019. 2, 8, 14, 15

[38] Nian Liu and Junwei Han. A deep spatial contextual long-term recurrent convolutional network for saliency detection. *IEEE Transactions on Image Processing (TIP)*, 2018. 1, 2

[39] Yufan Liu, Songyang Zhang, Mai Xu, and Xuming He. Predicting salient face in multiple-face videos. In *Proceedings of the IEEE Conference on Computer Vision and Pattern Recognition (CVPR)*, 2017. 3

[40] K. Min and J. Corso. TASED-Net: Temporally-aggregating spatial encoder-decoder network for video saliency detection. In *Proceedings of the IEEE International Conference on Computer Vision (ICCV)*, 2019. 2, 6, 12

[41] Parag Mital, Tim Smith, Robin Hill, and John Henderson. Clustering of gaze during dynamic scene viewing is predicted by motion. 2011. 2, 3, 6, 12

[42] Junting Pan, Cristian Canton Ferrer, Kevin McGuinness, Noel E O'Connor, Jordi Torres, Elisa Sayrol, and Xavier Giro-i Nieto. Salgan: Visual saliency prediction with generative adversarial networks. *arXiv*, 2017. 1, 2

[43] Robert J Peters, Asha Iyer, Laurent Itti, and Christof Koch. Components of bottom-up gaze allocation in natural images. 2005. 3

[44] Mikel D Rodriguez, Javed Ahmed, and Mubarak Shah. Action mach a spatio-temporal maximum average correlation height filter for action recognition. In *Proceedings of the IEEE International Conference on Computer Vision (ICCV)*. IEEE, 2008. 3

[45] Olga Russakovsky, Jia Deng, Hao Su, Jonathan Krause, Sanjeev Satheesh, Sean Ma, Zhiheng Huang, Andrej Karpathy, Aditya Khosla, Michael Bernstein, et al. Imagenet large scale visual recognition challenge. *International Journal of Computer Vision (IJCV)*, 2015. 15

[46] Michael J Swain and Dana H Ballard. Color indexing. 1991. 3

[47] Matthias Tangemann, Matthias Kümmerer, Thomas S.A. Wallis, and Matthias Bethge. Measuring the importance of temporal features in video saliency. In *Proceedings of the European Conference on Computer Vision (ECCV)*, 2020. [2](#), [3](#), [5](#), [8](#), [16](#)

[48] Eleonora Vig, Michael Dorr, and David Cox. Space-variant descriptor sampling for action recognition based on saliency and eye movements. In *Proceedings of the European Conference on Computer Vision (ECCV)*, 2012. [3](#)

[49] Wenguan Wang and Jianbing Shen. Deep visual attention prediction. *IEEE Transactions on Image Processing (TIP)*, 2017. [1](#), [2](#)

[50] W. Wang, J. Shen, F. Guo, M. Cheng, and A. Borji. Revisiting video saliency: A large-scale benchmark and a new model. In *Proceedings of the IEEE Conference on Computer Vision and Pattern Recognition (CVPR)*, 2018. [2](#), [3](#), [7](#), [13](#)

[51] Niklas Wilming, Torsten Betz, Tim C Kietzmann, and Peter König. Measures and limits of models of fixation selection. 2011. [3](#)

[52] Xinyi Wu, Zhenyao Wu, Jinglin Zhang, Lili Ju, and Song Wang. SalSAC: A video saliency prediction model with shuffled attentions and correlation-based convlstm. In *AAAI*, 2020. [2](#)

[53] Saining Xie, Chen Sun, Jonathan Huang, Zhuowen Tu, and Kevin Murphy. Rethinking spatiotemporal feature learning: Speed-accuracy trade-offs in video classification. In *Proceedings of the European Conference on Computer Vision (ECCV)*, 2018. [2](#), [3](#)

[54] Ruohan Zhang, Calen Walshe, Zhuode Liu, Lin Guan, Karl S. Muller, Jake A. Whritner, Luxin Zhang, Mary M. Hayhoe, and Dana H. Ballard. Atari-head: Atari human eye-tracking and demonstration dataset, 2019. [3](#)

[55] Bolei Zhou, Agata Lapedriza, Aditya Khosla, Aude Oliva, and Antonio Torralba. Places: A 10 million image database for scene recognition. *IEEE Transactions on Pattern Analysis and Machine Intelligence (TPAMI)*, 2017. [15](#)

Noise-Aware Saliency Prediction for Videos with Incomplete Gaze Data (Supplementary)

1. Derivation of the NAT cost function

Let's assume that $d(x_i, \tilde{x}_i)$ is a random variable with Gaussian distribution, $d(x_i, \tilde{x}_i) \sim G(\mu, \sigma^2)$, where $\mu = E[d(x_i, \tilde{x}_i)]$ indicates its average value, whereas $\sigma^2 = \text{Var}[d(x_i, \tilde{x}_i)]$ is its variance. When the predicted saliency map \hat{x}_i is optimal, *i.e.* when $\hat{x}_i = x_i$, $d(\hat{x}_i, \tilde{x}_i)$ has the same statistical distribution of $d(x_i, \tilde{x}_i)$, therefore for a perfectly working saliency map predictor, we can write $d(\hat{x}_i, \tilde{x}_i) \sim G(\mu, \sigma^2)$. Notice that, in the context of NAT, μ and σ are supposed to be known, whereas \hat{x}_i is the unknown. The likelihood of measuring $d(\hat{x}_i, \tilde{x}_i)$ is given by:

$$p[d(\hat{x}_i, \tilde{x}_i)] = \frac{1}{\sqrt{2\pi\sigma}} e^{-\frac{[d(\hat{x}_i, \tilde{x}_i) - \mu]^2}{2\sigma^2}}, \quad (1)$$

whereas for an entire dataset containing N saliency maps, we can write the negative log likelihood function as:

$$\begin{aligned} J(\hat{x}_0, \hat{x}_1, \dots, \hat{x}_N) &= -\ln \prod_i \frac{1}{\sqrt{2\pi\sigma}} e^{-\frac{[d(\hat{x}_i, \tilde{x}_i) - \mu]^2}{2\sigma^2}} = \\ &= \sum_i -\ln \left\{ \frac{1}{\sqrt{2\pi\sigma}} e^{-\frac{[d(\hat{x}_i, \tilde{x}_i) - \mu]^2}{2\sigma^2}} \right\} = \\ &= \sum_i \left\{ \ln(\sqrt{2\pi\sigma}) + \frac{[d(\hat{x}_i, \tilde{x}_i) - \mu]^2}{2\sigma^2} \right\}. \end{aligned} \quad (2)$$

To maximize the likelihood of the predicted maps while training the saliency map predictor, one optimizes then:

$$\begin{aligned} (\hat{x}_0, \hat{x}_1, \dots, \hat{x}_N) &= \underset{(\hat{x}_0, \hat{x}_1, \dots, \hat{x}_N)}{\text{argmin}} J(\hat{x}_0, \hat{x}_1, \dots, \hat{x}_N) = \\ &= \underset{(\hat{x}_0, \hat{x}_1, \dots, \hat{x}_N)}{\text{argmin}} \sum_i \left\{ \ln(\sqrt{2\pi\sigma}) + \frac{[d(\hat{x}_i, \tilde{x}_i) - \mu]^2}{2\sigma^2} \right\}, \end{aligned} \quad (3)$$

which leads, under the removal of the terms that do not depend on $(\hat{x}_0, \hat{x}_1, \dots, \hat{x}_N)$, to:

$$(\hat{x}_0, \hat{x}_1, \dots, \hat{x}_N) = \underset{(\hat{x}_0, \hat{x}_1, \dots, \hat{x}_N)}{\text{argmin}} \sum_i \left\{ \frac{[d(\hat{x}_i, \tilde{x}_i) - \mu]^2}{\sigma^2} \right\}, \quad (4)$$

and thus to the definition of the NAT cost function:

$$\begin{aligned} J_{\text{NAT}}^{\text{ideal}} &= \sum_i \left\{ \frac{[d(\hat{x}_i, \tilde{x}_i) - \mu]^2}{\sigma^2} \right\} = \\ &= \sum_i \left\{ \frac{[d(\hat{x}_i, \tilde{x}_i) - \mathbb{E}[d(x_i, \tilde{x}_i)]]^2}{\text{Var}[d(x_i, \tilde{x}_i)]} \right\}. \end{aligned} \quad (5)$$

2. Analysis of approximation in Eq. 5,6

To analyze the accuracy of Eq. 5,6 in the main paper, we select a subset of the video frames from the DIEM

dataset that contains gaze data from more than 200 observers. Given the very large number of gaze fixations for these frames, we anticipate that the estimated human-saliency map \tilde{x} is very close to ground-truth saliency x [28], and therefore analyze the accuracy of Eq. 5,6 under the assumption that the > 200 -observer gaze maps of these frames represent x . From these 200-observer gaze maps (x), we sample a certain number (denoted as M) of gaze fixation locations followed by blurring to compute \tilde{x} . Then, we compute \tilde{x} by sampling M locations from \tilde{x} followed by blurring. Using multiple realizations of \tilde{x} and \tilde{x} , we estimate $\mathbb{E}[d(x, \tilde{x})]$, $\mathbb{E}[d(\tilde{x}, \tilde{x})]$, $\text{Var}[d(x, \tilde{x})]$, $\text{Var}[d(\tilde{x}, \tilde{x})]$. We find that the mean absolute percentage error (MAPE) in the approximation of $\mathbb{E}[d(x, \tilde{x})]$ (Eq. 5 in main paper) goes from 21% for $N = 5$, to 13% for $N = 15$, and down to 10% for $N = 30$. Similarly, MAPE in the approximation of $\text{Var}[d(x, \tilde{x})]$ (Eq. 6 in main paper) goes from 13% for $N = 5$, to 6% for $N = 15$, and down to 5% for $N = 30$. Note that a large under/over-estimation of $\mathbb{E}[d(x, \tilde{x})]$ and $\text{Var}[d(x, \tilde{x})]$ in Eq. 5,6 (main paper) may lead to overfitting to noisy data or sub-optimal convergence respectively using Eq. 7 (main paper) for training. This would result in poor performance of NAT compared to traditional training – which, as shown by the results, is not the case.

3. Additional Results (mentioned in Sec. 5)

We now report the additional experiments performed to compare NAT (Eq. 7 in main paper) to traditional training (Eq. 2 in main paper). Furthermore, we show typical gaze maps obtained through traditional training and NAT compared to the ground truth for TASED on the ForGED dataset in Fig. 1.

3.1. Dataset type and size

In this section, we continue reporting the results from Sec. 5.1 of the main paper, where we compared NAT vs. traditional training for different dataset types and sizes. Table 1 compares the performance of traditional training to NAT on an additional dataset, the DIEM dataset [41], for the TASED architecture [40], and using KLD as discrepancy. As done throughout Sec. 5 of the main paper, the evaluation is performed on videos with gaze data from *all* of the available observers (in contrast to training, for which a subset of observers are used, see Table 1 in main paper). In case of DIEM dataset, given that only 84 videos are available, we use 30 or 60 videos for training and report the results on the remaining 24 videos, which are also used as validation set. The number of observers for these videos

ranges from 51 to 219, which makes DIEM a very low-noise evaluation set [28]. Results on DIEM are consistent with those reported in the main paper, with NAT providing better metrics in evaluation when compared to traditional training when less training data (e.g., 30 videos) is available.

videos	obs.	train	KLD↓	CC↑	SIM↑	NSS↑	AUC-J↑
30	5	Eq. 2	0.641	0.698	0.591	3.517	0.922
		NAT	0.599	0.708	0.592	3.513	0.934
	15	Eq. 2	0.597	0.710	0.602	3.582	0.930
		NAT	0.583	0.718	0.607	3.627	0.932
	31	Eq. 2	0.576	0.724	0.614	3.663	0.925
		NAT	0.559	0.731	0.618	3.694	0.928
60	5	Eq. 2	0.528	0.735	0.619	3.709	0.933
		NAT	0.518	0.737	0.616	3.639	0.940
	15	Eq. 2	0.485	0.757	0.639	3.795	0.933
		NAT	0.493	0.754	0.635	3.792	0.936
	31	Eq. 2	0.476	0.759	0.641	3.821	0.938
		NAT	0.467	0.766	0.654	3.864	0.935

Table 1: Saliency metrics on DIEM, for TASED Net, training with KLD as discrepancy, and various number of training videos and observers. The best metrics between traditional training (Eq. 2 in main paper) and NAT are in bold.

3.2. Discrepancy functions

To further verify that NAT generalizes to different discrepancy functions (continuing Sec. 5.2 from main paper), we train and test TASED on LEDOV [26] with the fixation-based discrepancy function, $d = -0.1\text{NSS}$, and the combination of fixation and density-based discrepancy functions, $d = \text{KLD} - 0.1\text{CC} - 0.1\text{NSS}$ (which is a popular discrepancy function used in video-saliency research [14, 50]). The test set for LEDOV is used for all reported evaluations on LEDOV dataset, which contains gaze data from 32 observers per video.

Table 2 shows NAT vs. traditional training (Eq. 2 in main paper) using $d = -0.1\text{NSS}$. For this specific experiment, with traditional training we observe that adopting RMSprop as the optimizer (as done for all experiments in the paper) shows very fast convergence to very high NSS values. While this property of fast and optimal convergence of discrepancy function has proven useful for all experiments in the paper (see Sec. 4 for details), for this specific experiment the solution provided by RMSprop optimization shows poor generalization to all other saliency metrics. This behavior is alleviated to some extent by switching RMSProp with Stochastic Gradient Descent (SGD) for traditional training – but at the cost of poor convergence in terms of NSS. To show this, in Table 2, we report two sets of experiments for traditional training for each size of training dataset (one with SGD and another with RMSprop). With NAT, however, we observe a consistent optimal convergence due to the regularizing effect of the NAT formulation that prevents overfitting to dataset noise.

We further observe that using additional terms with NSS in the discrepancy function, such as with $d = \text{KLD} - 0.1\text{CC} - 0.1\text{NSS}$ overcomes some of the issues of training

with NSS alone. Table 3, 4 show the comparison of traditional training vs. NAT for this combined discrepancy function. A high NSS performance in this case is well-correlated with good performance in terms of other metrics. Furthermore we note that, the performance of NAT is superior to traditional training when less gaze data is available, with the gap between the two approaches closing in with more gaze data. Given our analyses of all of the experiments with various discrepancy functions and dataset types, our conclusion is that the performance of models trained with density-based discrepancy functions (e.g., KLD) is better for traditional training as well as NAT, with NAT showing consistent superior performance compared to traditional training.

videos	obs.	train	KLD↓	CC↑	SIM↑	NSS↑	AUC-J↑
100	5	Eq. 2, SGD	2.352	0.244	0.267	2.272	0.761
		Eq. 2, RMSprop	4.139	0.192	0.056	9.92	0.178
		NAT	1.746	0.428	0.230	2.358	0.916
	30	Eq. 2, SGD	2.302	0.258	0.275	2.661	0.775
		Eq. 2, RMSprop	3.593	0.247	0.111	13.628	0.423
		NAT	1.903	0.398	0.198	2.370	0.919
461	5	Eq. 2, SGD	2.777	0.317	0.232	4.464	0.612
		Eq. 2, RMSprop	4.00	0.241	0.062	14.617	0.206
		NAT	1.305	0.575	0.354	3.29	0.929
	30	Eq. 2, SGD	2.252	0.470	0.355	2.463	0.593
		Eq. 2, RMSprop	3.526	0.292	0.127	14.048	0.381
		NAT	1.402	0.571	0.310	2.933	0.927

Table 2: Comparison of traditional training (Eq. 2 in main paper) vs. NAT on LEDOV testing set, for TASED Net, trained with -0.1NSS as discrepancy, and various number of training videos and observers. The best metric between each set of 3 experiments for a given dataset size (videos and observers) is in bold and the second-best is italicized. Given the strong overfitting behavior of NSS with traditional training using RMSprop for this particular set of experiments, we report traditional training optimized with SGD as well.

videos	obs.	train	KLD↓	CC↑	SIM↑	NSS↑	AUC-J↑
30	5	Eq. 2*	2.155	0.195	0.198	1.007	0.793
		NAT*	1.431	0.428	0.378	2.082	0.884
		Eq. 2	1.652	0.446	0.261	2.269	0.871
	30	Eq. 2	1.243	0.494	0.394	2.491	0.900
		NAT	1.149	0.540	0.423	2.782	0.905
		Eq. 2	1.368	0.496	0.395	2.430	0.863
100	5	Eq. 2	1.261	0.534	0.368	2.658	0.903
		NAT	1.034	0.574	0.432	3.250	0.928
		Eq. 2	1.261	0.534	0.368	2.658	0.903
	30	Eq. 2	1.159	0.577	0.485	3.912	0.864
		NAT	0.852	0.626	0.513	3.451	0.931
		Eq. 2	0.913	0.626	0.513	5.743	0.910
461	5	Eq. 2	1.159	0.577	0.485	3.912	0.864
		NAT	0.852	0.626	0.513	3.451	0.931
		Eq. 2	0.913	0.626	0.513	5.743	0.910
	30	Eq. 2	0.755	0.688	0.554	3.559	0.930
		NAT	0.755	0.688	0.554	3.559	0.930

Table 3: Saliency quality metrics on LEDOV testing set, for TASED Net, training with KLD-0.1CC-0.1NSS as discrepancy, and various number of training videos and observers. The best metrics between traditional training (Eq. 2 in main paper) and NAT are in bold. * Because of instability in training, in the 30 videos / 5 observers case we use KLD-0.1CC.

3.3. DNN architectures

To further verify that NAT works effectively on different DNN architectures, independently from the adopted dataset,

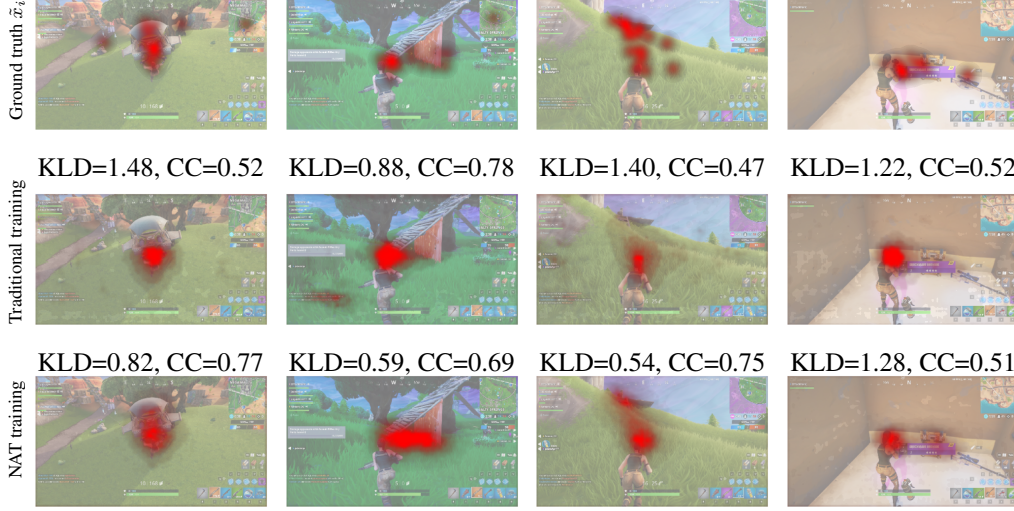


Figure 1: Typical gaze maps obtained through traditional training (second row – Eq. 2 in main paper) and NAT (third row) compared to the ground truth (first row) for TASED on the ForGED dataset, training with KLD loss, 30 training videos and 5 observers per frame (see Table 2 in main paper). Each panel reports in the title the corresponding KLD and CC values. The last column shows a failure case where the metrics KLD and CC indicate that NAT is worse than traditional training, although a visual inspection might indicate otherwise. *ForGED images have been published with the written permission of Epic Games.*

videos	obs.	train	KLD↓	CC↑	SIM↑	NSS↑	AUC-J↑
30	15	Eq. 2	0.687	0.696	0.590	3.618	0.900
		NAT	0.588	0.718	0.601	3.629	0.932
60	31	Eq. 2	0.555	0.727	0.609	3.605	0.935
		NAT	0.560	0.730	0.612	3.666	0.933
60	5	Eq. 2	0.555	0.728	0.615	3.660	0.930
		NAT	0.535	0.736	0.612	3.681	0.937
	15	Eq. 2	0.514	0.743	0.631	3.804	0.931
		NAT	0.488	0.755	0.636	3.814	0.939
	31	Eq. 2	0.502	0.748	0.639	3.887	0.931
		NAT	0.503	0.750	0.632	3.774	0.938

Table 4: Saliency quality metrics on DIEM testing set, for TASED Net, training with KLD-0.1CC-0.1NSS as discrepancy, and various number of training videos and observers. The best metrics between traditional training (Eq. 2 in main paper) and NAT are in bold.

we train SalEMA [37] on the ForGED dataset. We use KLD as the discrepancy function, with RMSprop as the optimizer with a learning rate equal to $1e^{-5}$ rather than Adam with learning rate $1e^{-7}$ and binary cross entropy as discrepancy function, as suggested by the authors (an analysis of this hyperparameter choice is discussed later). Consistently with the other cases analyzed here, the results in this case also suggest that NAT achieves better metrics than traditional training when the number of observers or videos is limited (Table 5).

4. Additional training details

Hyperparameters for TASED training on LEDOV. To ensure a fair comparison against traditional training and guarantee that the best performance are achieved for the

videos	obs.	train	KLD↓	CC↑	SIM↑	NSS↑	AUC-J↑
30	5	Eq. 2	1.723	0.348	0.279	1.7653	0.8705
		NAT	1.428	0.488	0.354	2.632	0.896
100	15	Eq. 2	1.497	0.479	0.356	2.672	0.886
		NAT	1.461	0.464	0.364	2.516	0.894
379	5	Eq. 2	1.454	0.458	0.444	2.825	0.903
		NAT	1.386	0.567	0.450	3.117	0.908
	2	Eq. 2	1.534	0.412	0.325	2.105	0.890
		NAT	1.44	0.450	0.345	2.327	0.901
	5	Eq. 2	1.052	0.612	0.462	3.237	0.912
		NAT	1.045	0.633	0.457	3.425	0.910

Table 5: Saliency quality metrics on ForGED testing set, for SalEMA, training with KLD as discrepancy, and various number of training videos and observers. The best metrics between traditional training (Eq. 2 in main paper) and NAT are in bold.

given architecture and dataset, we first perform some hyperparameter tuning of TASED on LEDOV with traditional training (Eq. 2 in main paper). We found that using RMSprop with a learning rate of 0.001 for KLD optimization gives better performance than the default settings originally proposed for training on DHF1K (*i.e.*, SGD with momentum 0.9 and learning rate 0.1 for decoder stepping down by a factor of 0.1 at iteration 750 and 950, and 0.001 for encoder), as shown in Table 6 and in Fig. 2. Thus, we adopt RMSprop with a learning rate of 0.001 to train TASED for both traditional training and NAT in all the experiments. An exception to this rule is the traditional training with SGD reported in Table 2, where we adopt SGD with a learning rate of 0.0001 (any higher leads to training instabilities due to data noise) and momentum 0.9.

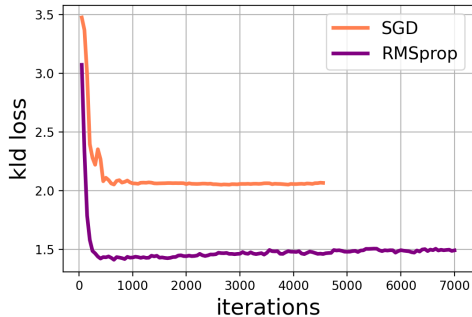


Figure 2: Validation-set performance plots (KLD vs. training iterations) for the LEDOV dataset during training of TASED with KLD as loss function and LEDOV dataset using: SGD, initial learning rate 0.1 for decoder and 0.001 for encoder, momentum 0.9 (default used by authors); and RMSprop, learning rate 0.001. Based on this experiment, we choose RMSprop with a learning rate of 0.001 for our experiments.

optimizer, learning rate, discrepancy	KLD \downarrow	CC \uparrow	SIM \uparrow	NSS \uparrow	AUC-J \uparrow
SGD, 0.1*, KLD	1.104	0.554	0.452	2.536	0.828
RMSprop, 0.001, KLD	0.671	0.736	0.587	4.262	0.934

Table 6: Performance on LEDOV for TASED trained traditionally using KLD with original settings, and those used in the main paper (RMSprop, learning rate 0.001) on the full LEDOV training set. We adopted the best hyperparameter setting (best metrics in bold) for all experiments. *Original settings: SGD, initial learning rate 0.1 for decoder and 0.001 for encoder, momentum 0.9.

Hyperparameters for SalEMA training on LEDOV. We train SalEMA [37] on the full LEDOV dataset with the default choice for loss function and optimizer (Adam optimizer, binary cross entropy, with learning rate $1e^{-7}$), and compare against the adoption of the RMSprop optimizer with KLD as the loss function and 2 learnings rates: $1e^{-5}$ and $1e^{-7}$ (see Table. 7). We train with LEDOV training set and we choose the best hyperparameter setting based on the LEDOV test-set performance for all of the experiments in the paper.

optimizer, learning rate, loss	KLD \downarrow	CC \uparrow	SIM \uparrow	NSS \uparrow	AUC-J \uparrow
Adam, $1e^{-7}$, BCE (original)	1.238	0.511	0.412	2.426	0.894
RMSprop, $1e^{-7}$, KLD	1.206	0.532	0.418	2.602	0.900
RMSprop, $1e^{-5}$, KLD	1.052	0.612	0.463	3.237	0.912

Table 7: Performance comparisons on LEDOV test set for SalEMA trained with the original hyperparameter settings and the ones used in this paper (RMSprop optimizer with $1e^{-5}$ learning rate) after training on LEDOV training set. Best metrics are in bold.

Details of training EML-Net. We train EML-Net [25] for image-saliency on our noisy version of SALICON train set [27] (generated by randomly selecting a subset 5 or 15 fixations per image, See Sec. 5.4 in main paper). To do so, we select the ResNet50 backbone [19]. Consistent with recommendations from authors, we train two versions of the encoder: first, we finetune starting from ImageNet-pretrained weights [45], and second, we finetune from Places365-pretrained weights [55]. The two saliency models obtained from the encoder-training stage are input to the decoder-training pipeline to give the final image-saliency predictor for EML-Net approach. We adopt the EML loss (which is a combination of KLD, CC and NSS losses described by authors) for training both traditionally (Eq. 2 in main paper) and using NAT. After searching through learning rates and optimizers, we find the author-specified choices to be most optimal: SGD with momentum with a learning rate of 0.01 at the beginning and multiplied by 0.1 after every epoch. We train both encoder and decoder for 10 epochs. After training, the best model for each experiment in Table 7 of the main paper is selected based on validation-set performance (using *all* available fixations on images in validation set), and submitted to SALICON benchmark for evaluation on the test set [27]. Note that even though the training is performed on few-fixation images to simulate a noisy version of the SALICON dataset, the evaluation on test set and validation set contains *all* of the available fixations.

5. Alternative methods to estimate \tilde{x} : additional details

In Sec. 5.4 of main paper, we discuss an alternative strategy using Gaussian kernel density estimation (KDE) with uniform regularizer to estimate \tilde{x} for training, instead of the common practice of blurring human gaze fixation locations using a Gaussian blur kernel of size approximately 1° viewing angle. We provide further details here. We estimate the optimal KDE bandwidth for *each* video frame, mixed with a uniform regularizer whose coefficient is also a parameter to be estimated. We do a per-frame estimation of optimal KDE bandwidth and mixing coefficient, to account for the general case where each frame can have a different variety of points of interest to attract gaze which cannot be explained with the optimal KDE bandwidth of another frame. The alternative to this is to estimate an optimal KDE bandwidth independent of the video frames, which amounts to the trivial case of obtaining a universal Gaussian-blur kernel of a different size. In this case, the treatment of the underlying gaze data for obtaining the measured saliency maps remains the same, in principle, as our experiments with $\sim 1^\circ$ viewing-angle Gaussian-blur kernel (which amounts to 36 pixels and 1920×1080 resolution for ForGED). To demonstrate this for completeness, in Table 8, we show some of the results

for TASED trained with ForGED and KLD as discrepancy. For this experiment, the training gaze maps are estimated using a Gaussian-blur kernel of size 27 pixels (at resolution 1920×1080), which amounts to $\sim 0.75^\circ$ viewing angle. We note in Table 8 that NAT outperforms traditional training, consistent with our experiments with $\sim 1^\circ$ viewing-angle Gaussian-blur kernel reported in the main paper.

videos	obs.	train	KLD↓	CC↑	SIM↑	NSS↑	AUC-J↑
30	2	Eq. 2	1.586	0.471	0.329	2.832	0.878
		NAT	1.387	0.546	0.378	3.153	0.879
	5	Eq. 2	1.358	0.563	0.345	3.184	0.903
		NAT	1.239	0.565	0.406	3.272	0.905
	15	Eq. 2	1.056	0.622	0.483	3.682	0.902
		NAT	1.035	0.616	0.476	3.757	0.917
100	5	Eq. 2	1.085	0.634	0.464	3.770	0.903
		NAT	1.018	0.636	0.474	3.633	0.926
379	5	Eq. 2	0.959	0.651	0.480	3.652	0.931
		NAT	0.888	0.670	0.517	4.091	0.924

Table 8: Performance comparisons on ForGED test set for TASED trained with KLD as discrepancy. Instead of computing gaze maps for train set with Gaussian blur kernel of size approximately 1° viewing angle (which amounts of 36 pixels at 1920×1080 resolution), we use a Gaussian blur kernel of size approximately 0.75° viewing angle (27 pixels). As we can see, the conclusion regarding the superior performance of NAT compared to traditional training applies independent of blur kernel size.

To estimate the optimal bandwidth using KDE, we optimize a gold-standard model for saliency prediction, which predicts the probability of fixation for one observer, given the gaze data from the remaining observers for the video frame (leave-one-out cross-validation) [34, 47]. We observe that, when gaze fixation locations are sparsely distributed across a frame, the optimal bandwidth for KDE is high, which would result in high-spread, almost-uniform saliency maps. Independent of the estimation strategy for \tilde{x} , we posit that there is an underlying uncertainty / noise in the measured saliency map – which is accounted for during training using NAT, to obtain improved performance over traditional training.

6. Overfitting behavior with NAT

Figure 3 shows the training and validation set performance (in terms of KLD) as a function of the training iteration when training TASED on LEDOV dataset with KLD discrepancy, for different number of observers and videos in the training set. For both the traditional approach (dashed orange line) and NAT (dashed purple line), the training-set curves decrease regularly, as expected in a smooth optimization process. However, the validation-set curves for traditional training (continuous orange line) quickly reach a minimum and then start diverging towards a higher asymptotic value, which is a clear sign of overfitting. On the other hand, the validation curves for NAT (continuous purple line) are always lower (suggesting better performance) and

tend to stabilize around asymptotic values without growing anymore — a clear sign, in this case, that overfitting is avoided. Note that for the training-set curves (dashed lines), the human saliency map used for KLD computation is derived using the limited number of observers available during the specific training experiment. As an additional check for the overfitting behavior of traditional training, we plot the performance of training set when compared against human saliency maps obtained from *all* the observers available in the training videos (32). These are indicated with dash-dotted lines. For few-observer experiments, the performance of traditional training on all-observer evaluations gets worse with increasing iterations. On the contrary, the performance on validation set, training set, and all-observer training set do not generally show signs of overfitting for NAT. Only in few cases, NAT plots are unstable at the beginning of the training (see the peaks in the validation curves in the left most panels for 30 observers trainings), but then the curves stabilize to an asymptotic value. The only exception to this is represented by the upper right panel in the figure (2-observer training with 461 videos), where we believe that the slight increase in the validation-set performance value is due to the approximation introduced in NAT to make it computable in practice. We observed a similar behavior when training on other datasets.

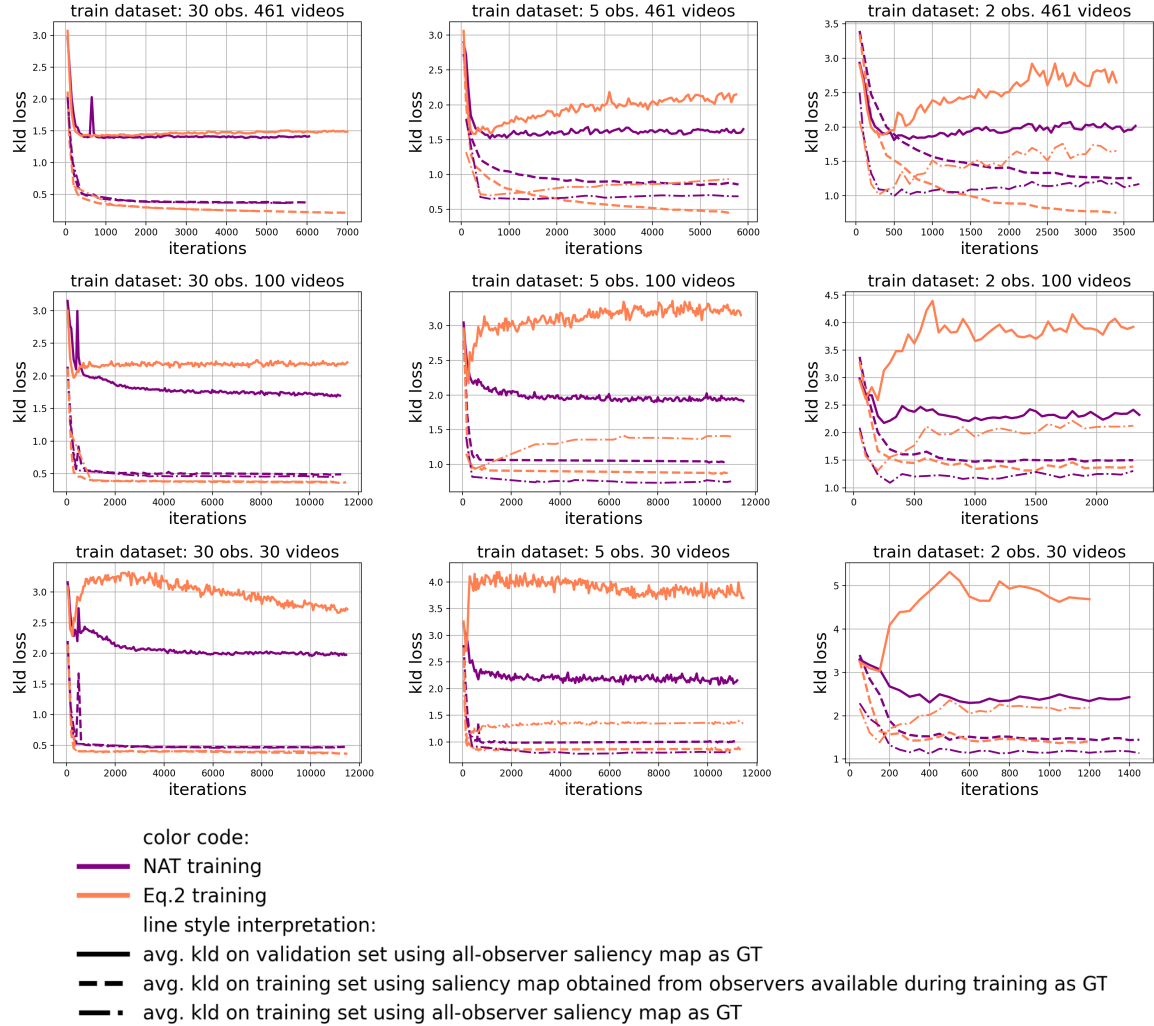


Figure 3: Training-set and validation-set KLD as a function of training iterations for TASED trained on LEDOV (“GT” in the legend indicates “ground-truth”). In contrast to the traditional training (Eq.2 in main paper), NAT does not overfit.